Cell Reports

Article

Structural basis of selective TRPM7 inhibition by the anticancer agent CCT128930

Graphical abstract

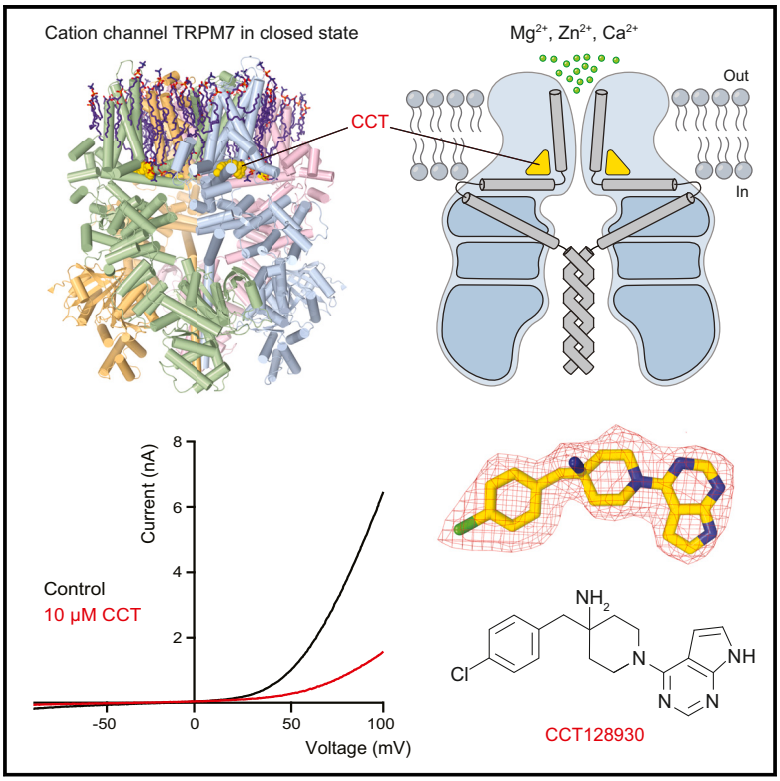

Highlights

- Cryo-EM structures of TRPM7 channel in complex with anticancer drug CCT128930
- CCT128930 binds to TRPM7 VL site and stabilizes the closed state
- Key role of VL residues in selective CCT128930 inhibition of TRPM7 but not TRPM6

Authors

Kirill D. Nadezhdin, Leonor Correia, Alexey Shalygin, ..., Maria G. Kurnikova, Vladimir Chubanov, Alexander I. Sobolevsky

Correspondence

vladimir.chubanov@lrz.uni-muenchen.de (V.C.), as4005@cumc.columbia.edu (A.I.S.)

In brief

Nadezhdin et al. solve the structure of TRPM7 in complex with the anticancer drug CCT128930. Combining cryo-EM, functional analysis, and MD simulations, the authors show that CCT128930 binds to a vanilloid-like site and stabilizes the channel in the closed state, revealing the molecular mechanism of selective TRPM7 inhibition.

Nadezhdin et al., 2024, Cell Reports *43*, 114108
April 23, 2024
https://doi.org/10.1016/j.celrep.2024.114108

CellPress

Cell Reports

CellPress
OPEN ACCESS

Article

Structural basis of selective TRPM7 inhibition by the anticancer agent CCT128930

Kirill D. Nadezhdin,[1,5] Leonor Correia,[2,5] Alexey Shalygin,[3] Muhammed Aktolun,[4] Arthur Neuberger,[1] Thomas Gudermann,[2,3] Maria G. Kurnikova,[4] Vladimir Chubanov,[2,*] and Alexander I. Sobolevsky[1,6,*]

[1]Department of Biochemistry and Molecular Biophysics, Columbia University, New York, NY, USA
[2]Walther-Straub Institute of Pharmacology and Toxicology, LMU Munich, Munich, Germany
[3]Comprehensive Pneumology Center, a Member of the German Center for Lung Research (DZL), Munich, Germany
[4]Department of Chemistry, Carnegie Mellon University, Pittsburgh, PA, USA
[5]These authors contributed equally
[6]Lead contact
*Correspondence: vladimir.chubanov@lrz.uni-muenchen.de (V.C.), as4005@cumc.columbia.edu (A.I.S.)
https://doi.org/10.1016/j.celrep.2024.114108

SUMMARY

TRP channels are implicated in various diseases, but high structural similarity between them makes selective pharmacological modulation challenging. Here, we study the molecular mechanism underlying specific inhibition of the TRPM7 channel, which is essential for cancer cell proliferation, by the anticancer agent CCT128930 (CCT). Using cryo-EM, functional analysis, and MD simulations, we show that CCT binds to a vanilloid-like (VL) site, stabilizing TRPM7 in the closed non-conducting state. Similar to other allosteric inhibitors of TRPM7, NS8593 and VER155008, binding of CCT is accompanied by displacement of a lipid that resides in the VL site in the apo condition. Moreover, we demonstrate the principal role of several residues in the VL site enabling CCT to inhibit TRPM7 without impacting the homologous TRPM6 channel. Hence, our results uncover the central role of the VL site for the selective interaction of TRPM7 with small molecules that can be explored in future drug design.

INTRODUCTION

The transient receptor potential cation channel, subfamily M, member 7 (TRPM7) is a bifunctional protein containing a membrane-spanning cation channel fused to a cytosolic α-type kinase domain, which can be cleaved from the channel in some physiological settings.[1–3] Notably, TRPM7 and its close homolog TRPM6 are the only known examples of ion channels in vertebrate genomes covalently linked to protein kinases and, therefore, often referred to as channel-kinases.[1,4,5] TRPM7 forms a constitutively active channel permeable to Zn^{2+}, Mg^{2+}, and Ca^{2+} ions.[3,6–9]

Independent evidence indicates that the TRPM7 channel is highly active in cancer cells, serving as a prime route for the cellular uptake of divalent cations, especially Mg^{2+} ions.[6,7,9] Besides the homeostatic control of cellular Mg^{2+} levels, TRPM7 regulates multiple Zn^{2+}- and Ca^{2+}-dependent signaling pathways, which drive tumor progression.[1,6,8,10–12] Accordingly, inhibition of TRPM7 currents by pharmacological compounds has been shown to suppress the proliferation of various cancer cell types *in vitro* and in animal disease models.[13–17] Collectively, these findings identified TRPM7 as an emerging anti-tumor drug target.[13–17]

Several small molecules were found to act as potent inhibitors of TRPM7, including NS8593 (NS), VER155008 (VER), and CCT128930 (CCT).[18–20] Recently, cryo-EM structures of TRPM7 were solved in the active open and inactive closed states.[21,22] One of these studies[21] identified the site of NS and VER binding, located near the cytoplasmic side of the membrane at the interface between the S3, S4, S5 and TRP helices. It was referred to as a vanilloid-like (VL) site because the homologous site in the vanilloid subfamily TRP channels is known as the vanilloid site.[23,24]

Here, we describe the inhibition of TRPM7 by the anticancer agent CCT and show that this pharmacological agent inactivates TRPM7 without impacting the homologous TRPM6 due to fine structural differences in their VL sites. Collectively, our findings provide the molecular basis for selective pharmacological modulation of the TRPM7 channel.

RESULTS

Electrophysiological characterization of TRPM7 inhibition by CCT

TRPM7 is a constitutively active cation channel, negatively regulated by intracellular Mg^{2+}, that presumably binds at the intracellular entry to the ion channel pore.[7,25] Accordingly, the induction of whole-cell TRPM7 currents in the patch-clamp measurements is traditionally achieved by removing cytosolic Mg^{2+} with EDTA added to the patch pipette solutions.[7,25] We used this approach to study the inhibitory effect of CCT (Figure 1A) on full-length TRPM7 transiently expressed in HEK293T cells. As expected,

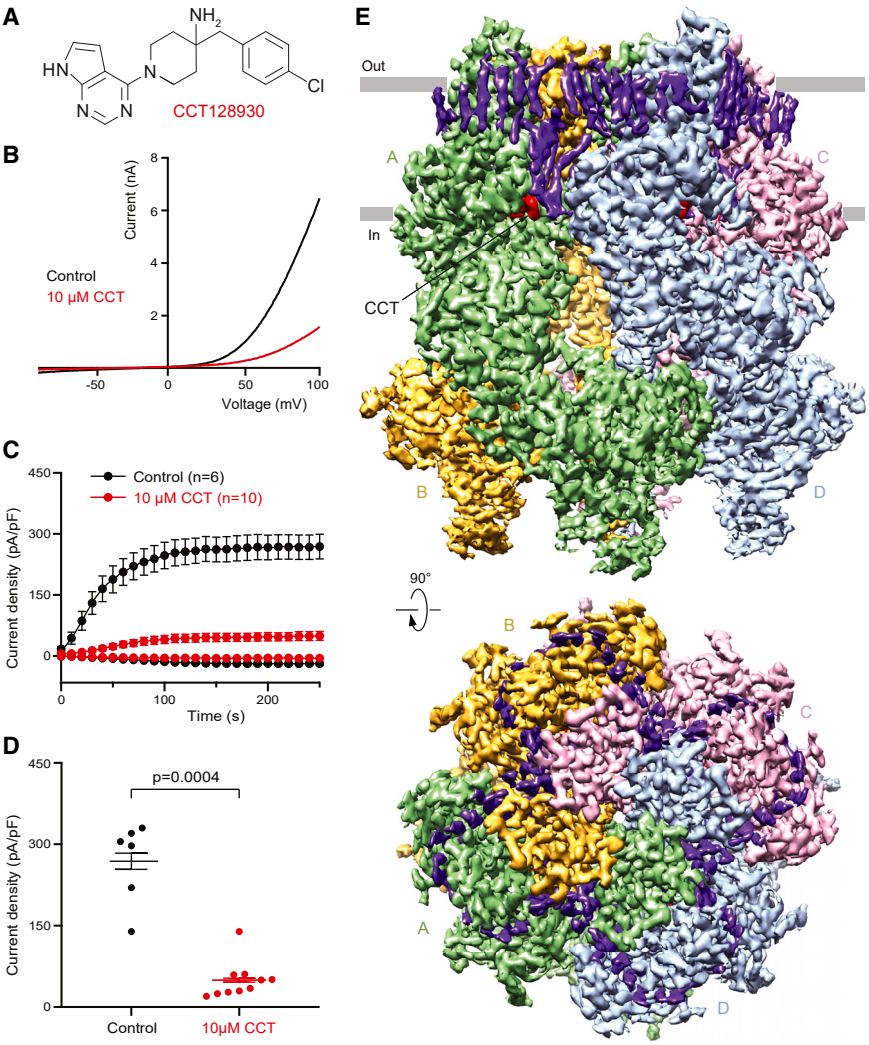

Figure 1. Electrophysiological and cryo-EM characterization of TRPM7 in the presence of CCT

(A) Chemical structure of CCT.

(B) Representative current-voltage (I-V) relationship of fully developed whole-cell currents measured in HEK293T cells expressing TRPM7 in the absence (black) and presence (red) of 10 μM CCT.

(C) Time dependence of the average current density measured at −80 and +80 mV during experiments illustrated in (B). Data are mean ± SEM; *n*, the number of biological replicates (cells examined).

(D) Dot plot showing average current density recorded at +80 mV at 250 s in (C). The *p* value is given for the U test (Mann-Whitney). Data are mean ± SEM. Source data are provided.

(E) Cryo-EM map of $TRPM7_{CCT}$ at 2.45 Å resolution, viewed parallel to the membrane (top) and extracellularly (bottom), with the density for TRPM7 subunits colored green, beige, pink, and blue, CCT in red and lipids in purple. See also Figures S1–S3 and Table S1.

TRPM7 currents displayed an amplitude increase during the first ~2 min of recordings (Figures 1B and 1C). The current-voltage (I-V) relationship for fully developed TRPM7 currents showed a characteristic shape with a reversal potential of approximately 0 mV, steep outward rectification, and negligibly small inward currents (Figure 1B). After addition of 10 μM CCT to the recording chamber, the TRPM7 current amplitude was dramatically reduced (Figures 1C and 1D). Alternatively, TRPM7 currents were inhibited when the cells were perfused with 10 μM CCT after the saturation of channel activation had been reached (Figure S1A). In the same experimental settings, 10 μM CCT did not affect the amplitude of currents mediated by TRPM6, the closest homolog of TRPM7 (Figures 2A–2C and S1C). Moreover, 10 μM CCT did not inhibit the activity of TRPM3 or TRPM8, the more distal members of the TRPM channel family (Figure 3), supporting the notion that CCT is a selective inhibitor of TRPM7.

Cryo-EM of TRPM7-CCT complex

To investigate the molecular basis of TRPM7 inhibition by CCT, we determined a cryo-EM structure of the $TRPM7_{CCT}$ complex. For these structural studies, we used a C-terminally truncated mouse TRPM7 construct, which represents a functional channel with the proteolytically cleaved kinase domain.[2] We extracted TRPM7 from the membranes of HEK293S cells using the glyco-diosgenin detergent, reconstituted the protein into lipid nanodiscs, and subjected it to cryo-EM in the presence of 400 μM CCT. Cryo-EM analysis of this sample resulted in a 2.45-Å resolution map, with clear density for four protein subunits surrounded by annular lipids (Figures 1, S2, and S3; Table S1).

The tetrameric $TRPM7_{CCT}$ has a structural architecture typical of other TRPM channels[1] (Figure 4A). Each TRPM7 subunit consists of an intracellular N-terminal domain, which includes four melastatin homology regions (MHR1-4), a transmembrane domain (TMD) composed of six transmembrane helices (S1-S6), a pore loop (P loop) between S5 and S6, and a cytosolic C-terminal domain (CTD). The amphiphilic TRP helix runs nearly parallel to the membrane and connects the TMD to the CTD.

CCT binds to the VL site

Inspection of the cryo-EM map revealed four identical densities, one per subunit of $TRPM7_{CCT}$ tetramer, with the characteristic shape of CCT (Figures 1E, 4A, and 4B). Each of these densities unambiguously identifies CCT binding sites located in the TMD region that faces the cytoplasmic leaflet of the membrane, at the interfaces between the S1-S4 and pore domains, atop the TRP helix (Figure 4C). Each site is contributed by the N-terminal part of S3 (residues D922, Y923, and F924), the C-terminal part

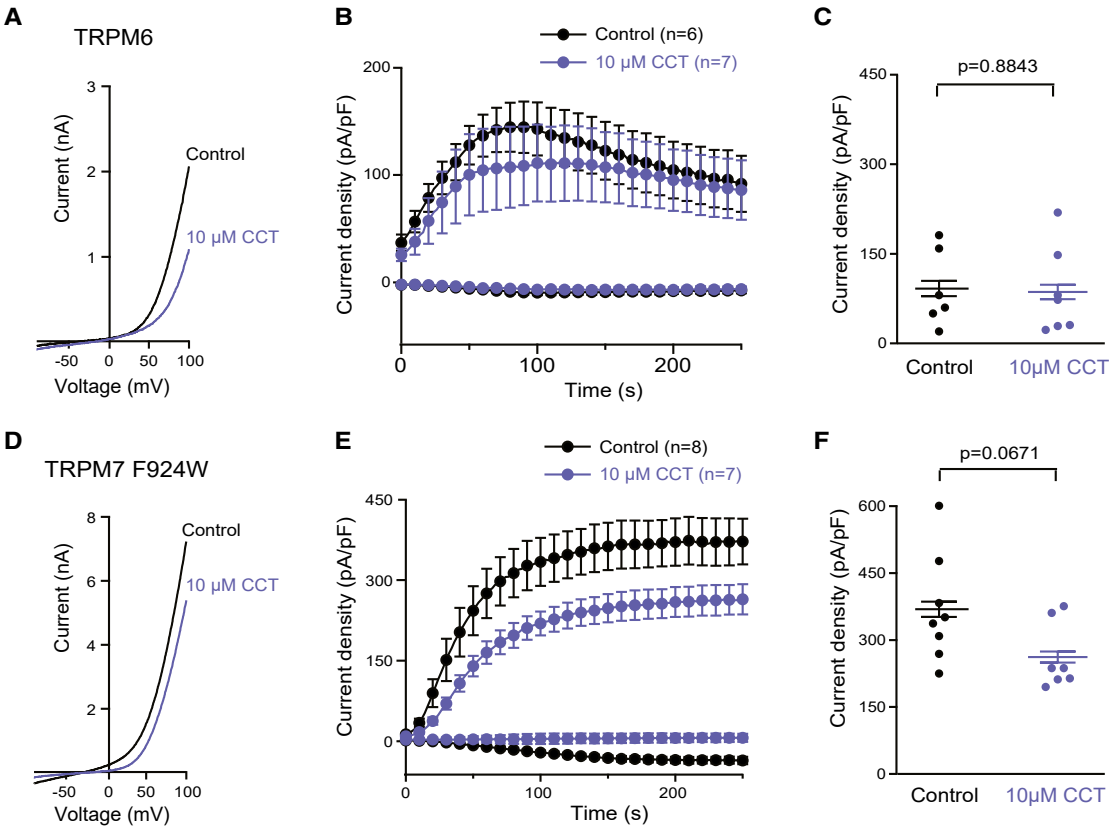

Figure 2. Electrophysiological characterization of TRPM6 and mutant TRPM7 channel in the presence of CCT

(A and D) Representative current-voltage (I-V) relationships of fully developed whole-cell currents measured in HEK293T cells expressing TRPM6 (A) and TRPM7-F924W (D) in the absence (black) and presence (blue) of 10 μM CCT.

(B and E) Time dependence of the average current density measured at −80 and +80 mV in the absence (black) or presence (blue) of 10 μM CCT in experiments illustrated in (A) and (D), respectively. Data are mean ± SEM; *n*, the number of biological replicates (cells examined).

(C and F) Dot plots showing the average density of outward current recorded at +80 mV at 250 s in the absence (black) and presence (blue) of 10 μM CCT from HEK293T cells expressing TRPM6 (C) and TRPM7-F924W (F). The *p* values are shown for the unpaired t test with Welch's correction (C) or U test (F). Data are mean ± SEM. Source data are provided. See also Table S2.

of S4 (D978 and A981), S4-S5 linker (M991), and TRP helix (W1111, Q1114, and F1118). The inhibitor-channel interactions are mostly hydrophobic, except for the hydrogen bond between the piperidine-amine of CCT and the carboxyl group of the D922 side chain (Figure S4A and S5). Since the homologous site in TRPV channels is known as the vanilloid site, we will refer to this site as VL.[21,23]

To verify that inhibition of TRPM7 by CCT is mediated by the VL site, we mutated residues contributing to CCT binding and compared inhibition of Ca^{2+} influx in cells expressing the wild-type channel and TRPM7 variants with point mutations of residues in the VL site (Figure 4D; Table S2). The half-maximal inhibitory concentration (IC_{50}) for wild-type TRPM7 was 1.42 ± 0.01 μM (*n* = 6). In line with the structural data, the A981V, A981L, and W1111A substitutions fully abolished the inhibitory effect of CCT (Figure 4D). We noted that the TRPM7 residues D922 and F924 are not conserved and that the CCT-insensitive channel TRPM6 contains glutamate and tryptophan at these positions (E914 and W916 in mouse TRPM6) (Figure S6A). Therefore, we studied whether the D922E and F924W substitutions in TRPM7 impact the inhibitory effect of CCT.

CCT inhibition of the D922E mutant was very weak, and it was not feasible to calculate the IC_{50} value in the working range of CCT concentrations (Figure 4D), likely due to the elongated side chain of glutamate compared with aspartate being no longer capable of establishing a hydrogen bond with the piperidine-amine of CCT. In addition, we found that TRPM7-F924W showed no response to CCT application (Figure 4D), probably because of the direct interference of the larger side chain of W924 with CCT binding to the VL pocket. In line with this idea, the potency of TRPM7-F924A inhibition by CCT was only modestly reduced (IC_{50} = 2.32 ± 0.02 μM) (*n* = 3) (Figure 4D; Table S2). Moreover, the F924W substitution did not alter the activating potency of the agonist naltriben (NTB)[26] (Figure S6B; Table S2), indicating that F924W affected the interaction of CCT with the VL site without an overall impact on TRPM7 activation. Overall, these results support the idea that the VL site mediates CCT inhibition of TRPM7 and that the side chains of F924 and D922 serve as the

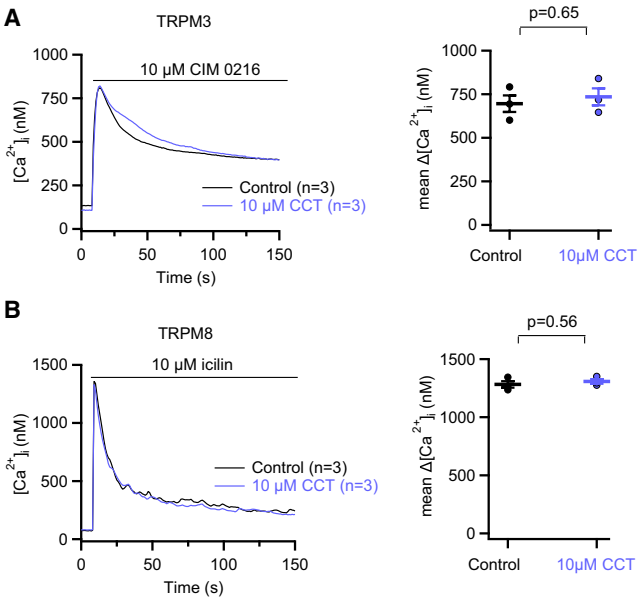

Figure 3. Assessment of the TRPM3 and TRPM8 channels expressed in HEK293T cells

Left panels: intracellular Ca^{2+} levels ($[Ca^{2+}]_i$) in TRPM3-expressing cells upon external application of 10 μM CIM 0216 (A) and in TRPM8-expressing cells exposed to 10 μM icilin (B) in the absence (control) or in the presence of 10 μM CCT. Representative traces are shown from $n = 3$ independent experiments (technical replicates). Right panels: Ca^{2+} rises ($\Delta[Ca^{2+}]_i$, mean ± SEM, $n = 3$, technical replicates) were calculated from measurements shown in the left panels by subtraction of the resting $[Ca^{2+}]_i$ from the maximal $[Ca^{2+}]_i$ after the application of agonists. The p values are shown for the unpaired t test. Source data are provided.

crucial selectivity factors in the corresponding inhibitory mechanism.

Comparative analysis of TRPM7 structures in complex with CCT and other modulators

To compare the effect of inhibitor binding on the ion channel pore, we measured the pore radius in $TRPM7_{CCT}$ and compared it with the pore radius in the previously solved structures of TRPM7 obtained in the absence of ligands ($TRPM7_{apo}$) or in complex with its pharmacological modulators VER ($TRPM7_{VER}$), NS ($TRPM7_{NS}$), and NTB ($TRPM7_{NTB}$).[21] The pore radius of TRPM7 has two narrow constrictions: one at the selectivity filter and the second at the gate region that allows or stops permeation of water and ions through the pore (Figure 5A). The pore radius profile of $TRPM7_{CCT}$ is very similar to the ones previously obtained for $TRPM7_{apo}$, $TRPM7_{VER}$, and $TRPM7_{NS}$ (Figure 5B), indicating that the CCT-bound structure represents the closed, non-conducting state. This pore profile is in stark contrast with the profile obtained for the open-state structures of TRPM7, activated as a result of either the introduced gain-of-function mutation N1098Q ($TRPM7_{N1098Q}$) or binding of agonist NTB ($TRPM7_{NTB}$),[21] where the gate region is substantially wider (Figure 5B). Therefore, we propose that, in analogy to VER and NS, CCT acts by allosterically stabilizing the closed state of the TRPM7 channel.

Further analysis of $TRPM7_{apo}$ revealed that the VL site accommodates the acyl chain of an annular lipid molecule (Figure 6A). Upon CCT binding (Figure 6B), this acyl chain disappeared, suggesting that CCT outcompeted the lipid from the VL site. A similar situation was observed for two other TRPM7 inhibitors that act through the VL site, VER and NS (Figures 6C, 6D, S4B, and S4C),[21] suggesting that the replacement of endogenous lipids by pharmacological agents in the VL site is a common step of the TRPM7 channel inhibition. While we modeled the VL site lipid in $TRPM7_{CCT}$ as an acyl chain of phosphatidylcholine, it could be another type of phospholipid. Determining the precise chemical nature of the VL site lipid will require additional investigation.

Interestingly, NS inhibits both TRPM7 and TRPM6.[18,19] In contrast, VER resembles CCT, because this compound acts as a potent inhibitor of TRPM7 but is inactive against TRPM6.[18] Therefore, we compared the impact of the TRPM6-like mutation F924W on the capability of VER and NS to inhibit TRPM7. Analogously to the situation with CCT (Figure 4D), the F924W mutation caused a 19-fold increase in the IC_{50} for VER (Figure 6E; Table S2). However, F924W elicited only a moderate impact on the action of NS (Figure 6F; Table S2). These findings are in agreement with the model that the side chains of F924 and W924 differently interfere with the VER and NS binding to the VL site of TRPM7 (Figures 6C, 6D, S4B, S4C, and S5). Taken together, we concluded that F924 represents the critical structural determinant of the specificity of CCT and VER effects on TRPM7 versus TRPM6.

MD simulations of TRPM7 in complex with antagonists

To further validate CCT binding to the VL site and to probe the contribution of different residues to inhibitor binding, the TMD of TRPM7 in the closed conformation was placed in POPC lipid bilayer and water electrolyte solution at room temperature and subjected to 800- to 950-ns all-atom equilibrium MD simulations (Figures 7, S7A, and S7B). We first compared the behavior of the VL site in the absence (apo) and presence of CCT. In the apo state, the structure was stable and showed high occupancy of the VL site by an acyl chain of a POPC lipid (Figure 7A), residing in a similar position to the cryo-EM structure (Figure 6A). We also observed a continuous presence of two lipid molecules, cholesterol, which was modeled according to the cryo-EM structure, and a phospholipid near the VL site that entered the structure during simulation (Figure 7A). Consistent with the cryo-EM experiment (Figure 6B), binding of CCT was accompanied by displacement of the lipid from the VL site (Figure 7B). Interestingly, the resident cholesterol and the second POPC molecule remained at about the same place as in the apo structure simulation. The resident POPC contributed to the CCT binding, which is consistent with the cryo-EM structure (Figure 6B). Most importantly, the neighboring aspartate residues D922 and D978 showed high propensity to form a hydrogen bond to the nitrogen of CCT, providing an alternating hydrogen bond acceptor oxygen during most of the simulation time, which suggests their important role in CCT binding. In addition, the hydrogen bond and hydrophobic interaction with Y923 in the immediate proximity to F924 supports the important role of F924 in selective binding of inhibitors to the VL site in TRPM7 as suggested by the mutagenesis experiments

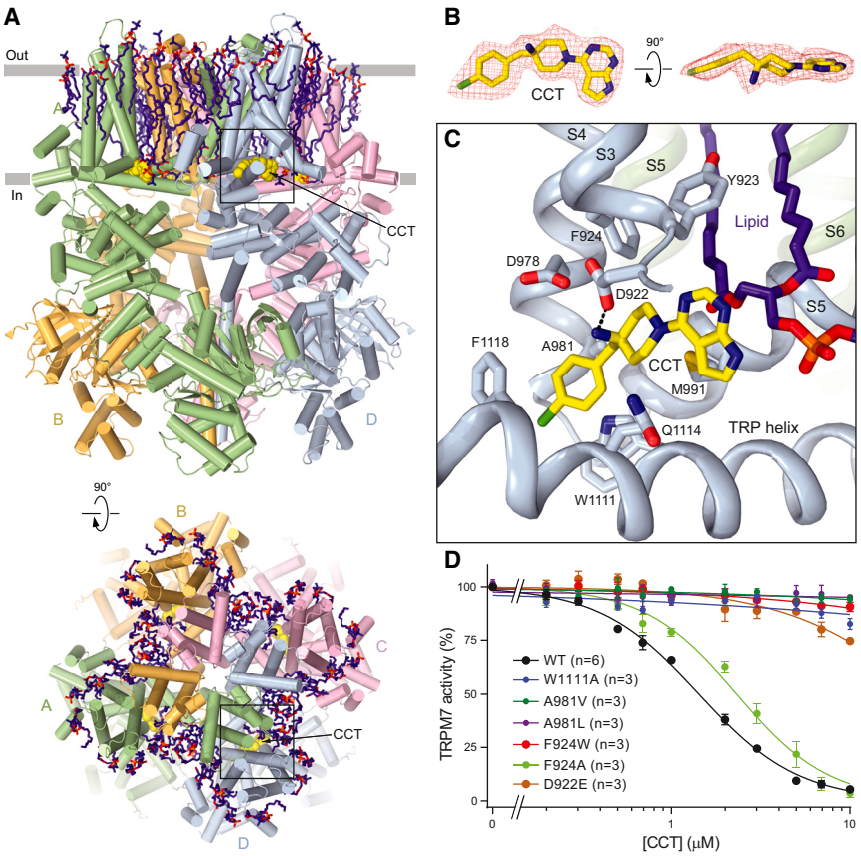

Figure 4. Structure of TRPM7$_{CCT}$ and CCT binding site

(A) Structure of TRPM7$_{CCT}$ viewed parallel to membrane (top) and extracellularly (bottom), with four subunits colored green, beige, pink, and blue, the molecules of CCT shown as space-filling models (yellow) and lipids as sticks (purple).

(B) Molecule of CCT viewed from two different angles, with the cryo-EM density shown as red mesh.

(C) Close-up view of the CCT binding site. The molecule of CCT (yellow) and residues involved in its binding, as well as the neighboring lipid (purple) are shown in sticks. The dashed line indicates a hydrogen bond between CCT and D922.

(D) Concentration-dependences for inhibition of wild-type (WT) and mutant TRPM7 channels by CCT. TRPM7 inhibition was determined using the Ca^{2+} influx assay. Curves through the points (mean ± SEM) are the logistic Equation 2 fits; *n*, the number of independent measurements (technical replicates). The corresponding values of IC_{50} and n_{Hill} are provided in Table S2. Source data are provided. See also Figure S4 and Table S2.

(Figures 2, 4D, 6E, 6F, and S1; Table S2). During MD simulations, we also observed that the hydrophobic residues W1111 and F1118 (TRP helix) and V982 (S4) form a water-excluding cage that is occupied by the lipid in the apo state but inhibitor in the inhibitor-bound state. At the same time, a continuous water channel formed at the side of the VL binding site (Figure S7C), suggesting a mechanism for the inhibitor access route in a solvated form.

We further verified the importance of the key residues in the VL site for the TRPM7 inhibition by running MD simulations with TRPM7 bound to VER and NS (Figures 7C, 7D, S7A, and S7B). Similar to CCT, the adjacent to the VL site phospholipid

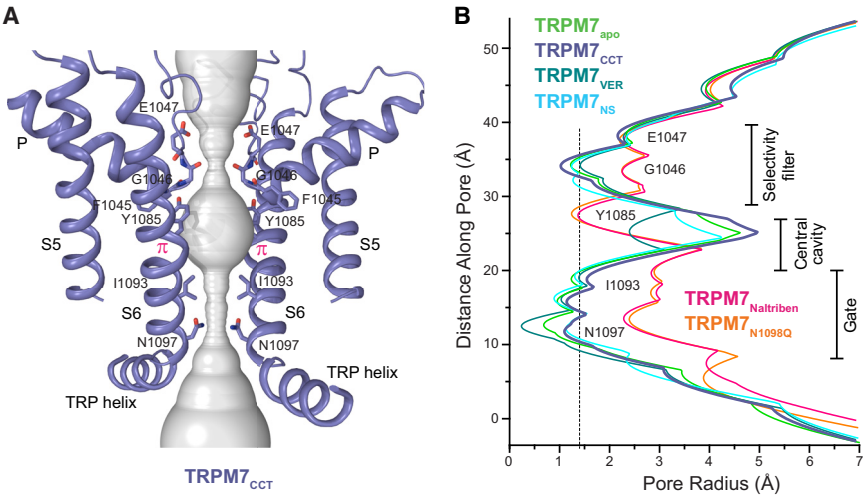

Figure 5. Pore in TRPM7$_{CCT}$ compared with other TRPM7 structures

(A) Pore-forming domain in TRPM7$_{CCT}$ with the residues contributing to pore lining shown as sticks. Only two of four subunits are shown, with the front and back subunits omitted for clarity. The pore profile is shown as a space-filling model (gray). The π-bulge in the middle of S6 is labeled.

(B) Pore radius for TRPM7$_{CCT}$ (slate) in comparison with the pore radius for TRPM7$_{apo}$ (green, PDB: 8SI3), TRPM7$_{VER}$ (teal, PDB: 8SI7), TRPM7$_{NS}$ (cyan, PDB: 8SIA), TRPM7$_{Naltriben}$ (pink, PDB: 8SI5), and TRPM7$_{N1098Q}$ (orange, PDB: 8SI4), all calculated using HOLE. The vertical dashed line denotes the radius of a water molecule, 1.4 Å.

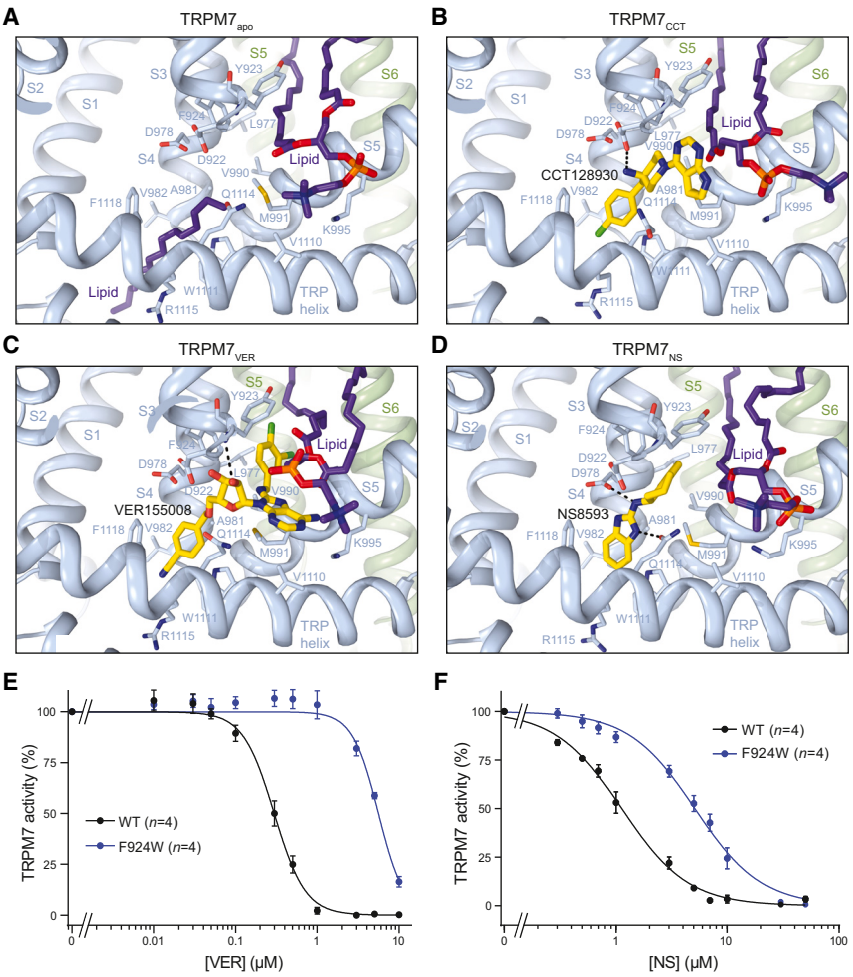

Figure 6. VL site in TRPM7

(A–D) Close-up view of the VL site in $TRPM7_{apo}$ (A, PDB: 8SI3), $TRPM7_{CCT}$ (B, this study), $TRPM7_{VER}$ (C, PDB: 8SI7), and $TRPM7_{NS}$ (D, PDB: 8SIA), with lipid (purple) and inhibitor (yellow) molecules as well as residues involved in their binding shown in sticks. The dashed lines in (B), (C), and (D) show hydrogen bonds between the pharmacological agents and side chains of residues contributing to the VL site.

(E and F) Concentration-dependences for inhibition of wild-type (WT) and mutant F924W TRPM7 channels by VER (E) and NS (F). TRPM7 inhibition was determined using the Ca^{2+} influx assay. Curves through the points (mean ± SEM) are the logistic Equation 2 fits; *n*, the number of independent measurements (technical replicates). The corresponding values of IC_{50} and n_{Hill} are provided in Table S2. Source data are provided. See also Figures S5 and S6; Table S2.

remained in close proximity and was also making direct contacts with the inhibitor molecules. Most importantly, the TRPM7 signature residues in the VL pocket, D922 and F924 (Figure S6A), were either directly involved in strong interactions (hydrogen bonds between VER or NS and D922 or D978) or surrounded by residues forming hydrophobic interactions with the inhibitors (F924 as well as A981, V982, M991, W1111, and F1118). The results of our MD simulations therefore provide strong support to binding of CCT, VER, and NS to the VL site and highlight the important role of the signature residues D922 and F924 in selective inhibition of TRPM7.

DISCUSSION

Here, we used cryo-EM to resolve the structure of TRPM7 in complex with the anticancer agent CCT ($TRPM7_{CCT}$). $TRPM7_{CCT}$ recapitulated the closed-state conformations of the TRPM7 structures in complex with alternative pharmacological inhibitors NS ($TRPM7_{NS}$) and VER ($TRPM7_{VER}$).[21] We concluded that $TRPM7_{CCT}$ represents the closed, non-conducting state of TRPM7. This study also discovers the mechanism of TRPM7 inhibition by CCT. The CCT-binding site in TRPM7 is formed by the N-terminal part of S3, the C-terminal part of S4, S4-S5 linker, and the TRP helix, and is referred to as the VL site because of its similar location to the vanilloid site initially identified in TRPV (vanilloid family) channels.[23] The analogous site was shown to bind the antagonist NDNA in TRPM5[27] and activator GNE551 in TRPA1.[28] Moreover, in our recent structural analysis of TRPM7, we found that two other structurally unrelated antagonists, VER and NS, also bind to the VL site of TRPM7.[21]

Structural analysis of TRPM7 in the absence of ligands ($TRPM7_{apo}$) revealed that the VL site contains the acyl chain of a lipid, which disappears upon CCT binding. Further studies are needed to determine the exact nature of the lipid present in the VL site. Intriguingly, the vanilloid-binding site of TRPV1 in the apo state contains phosphatidylinositol, which is also expelled upon binding of exogenous activators or inhibitors.[29,30] The vanilloid-binding pocket of TRPV3 contains a phospholipid, which is released upon activation by heat.[31] We hypothesized that binding any of the three structurally unrelated ligands to the VL site of TRPM7 outcompetes the endogenous lipid from the VL site. However, a functional interplay of the lipid and CCT in the regulation of the TRPM7 channel remains to be established.

Using mutagenesis, functional analysis, and MD simulations, we demonstrated the crucial impact of D922, F924, A981, and W1111 residues in the VL site on CCT inhibitory efficiency, thus confirming our structural model of TRPM7 inhibition. Furthermore, this combinatory approach uncovered a unique role of D922 and F924 in the selective regulation of the TRPM7 channel. Unlike other residues in the VL site, D922 and F924 are not conserved across TRPM channels and exchanged to glutamate and tryptophan in TRPM6 (Figure S6A), the closest homolog of TRPM7, which is insensitive to CCT and VER but

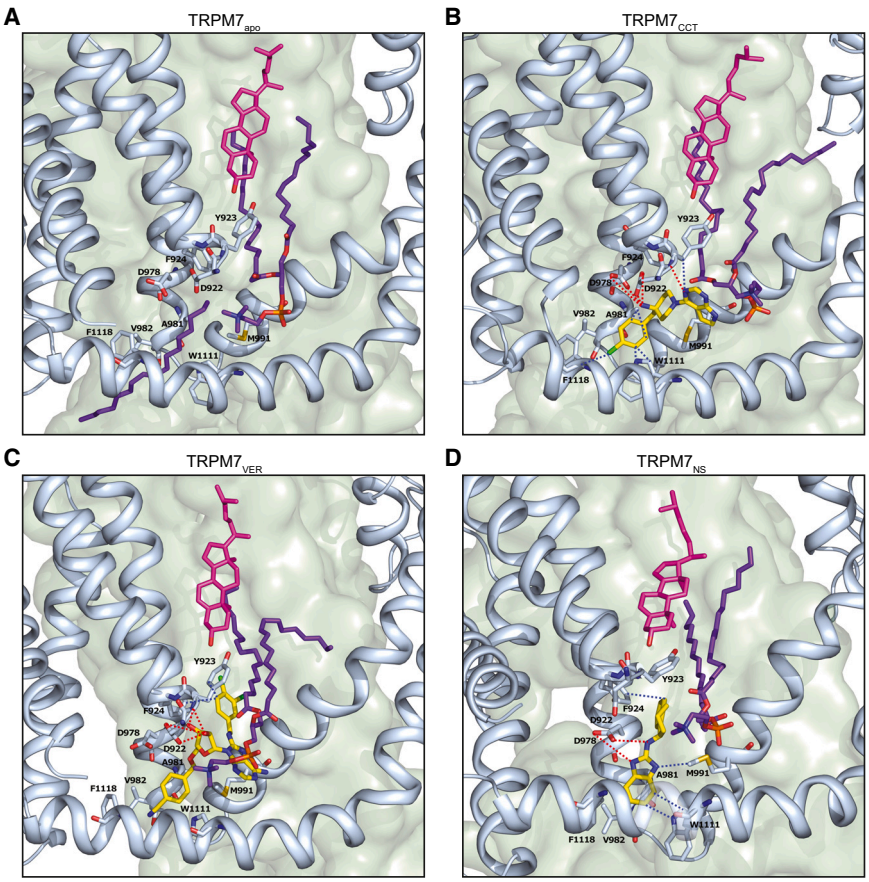

Figure 7. VL site representative structures from the MD simulations

Close-up view of the VL site after the MD simulations of $TRPM7_{apo}$ (A), $TRPM7_{CCT}$ (B), $TRPM7_{VER}$ (C), and $TRPM7_{NS}$ (D), with a lipid and inhibitor molecules (yellow) in the binding pocket as well as the residues involved in their binding shown in stick representation. The resident POPC lipid molecule shown in all panels in purple contributes to interaction with the inhibitors; the cholesterol molecule is shown in magenta. The VL binding site subunit is shown in colors matching the colors of Figure 6. The neighboring subunit on the back against which the POPC lipid tail resides is shown as a green surface. The dashed lines (red and blue) in (B), (C), and (D) show the most persistent atom contacts between the pharmacological agents and the protein. The red dashed lines show the hydrogen bonds between the inhibitors and the VL site residues, the blue dashed lines show the hydrophobic contacts between the inhibitors and the hydrophobic side chains of the protein residues. See also Figure S7.

shows a robust response to NS. We found that TRPM6-like F924W substitution in TRPM7 abolished the inhibitory effect of CCT, presumably because the larger side chain of W924 interferes with the binding of CCT to the VL site. In good agreement with this model, the adjacent to F924 residue Y923 was tightly interacting with the inhibitor throughout MD simulations (Figure 7), and CCT inhibition of TRPM7 was only modestly affected by the F924A mutation (Figure 4D). Such a structural impact of F924W also explains the distinct selectivity of NS and VER action on TRPM7 compared with TRPM6. Collectively, we propose that D922 and F924 are the structural determinants of selective pharmacological targeting of TRPM7.

Currently, the prevailing view is that TRPM7 represents the prime channel for the cellular uptake of divalent cations, including Mg^{2+}, Ca^{2+}, and Zn^{2+} ions.[1] Pharmacological modulators were used extensively to map the cellular role of TRPM7 in a broad range of experimental settings, including mouse models of human diseases.[14,16,32] One of the most prominent findings in this research area is the striking attenuation of proliferation of many types of cancer cells by TRPM7 inhibitors.[5,7,16,33–37] Consequently, TRPM7 has been suggested as a prospective anticancer target.[13,15] In addition, pharmacological modulation of TRPM7 appears to be beneficial for patients with immune, cardiovascular, and neurological disorders.[1] Accordingly, the presented TRPM7 structure in complex with CCT can serve as a template for the structure-based drug design to achieve selective regulation of TRPM7.

Limitations of the study

In structural experiments presented here, we used a C-terminally truncated mouse TRPM7 construct that lacks the cytosolic α-type kinase domain. Although the truncated part represents ~31% of the full-length TRPM7 polypeptide, the remaining part assembles into an entirely functional channel. Moreover, in certain physiological settings, the TRPM7 kinase domain is naturally cleaved from the channel.[1–3] Thus, our construct emulates the function of TRPM7 with the proteolytically cleaved kinase domain. The structural role of the kinase domain in TRPM7 awaits further investigations.

STAR★METHODS

Detailed methods are provided in the online version of this paper and include the following:

- KEY RESOURCES TABLE
- RESOURCE AVAILABILITY
  - Lead contact
  - Materials availability
  - Data and code availability

SUPPLEMENTAL INFORMATION

Supplemental information can be found online at https://doi.org/10.1016/j.celrep.2024.114108.

ACKNOWLEDGMENTS

We thank Robert Grassucci and Zhening Zhang (Columbia University Cryo-Electron Microscopy Center) and Vamseedhar Rayaprolu (Pacific Northwest Center for Cryo-EM, PNCC) for help with microscope operation and data collection. We thank Joanna Zaisserer and Anna Erbacher (Walther-Straub Institute, LMU Munich) for their technical assistance. Some of this work was performed at the Columbia University Cryo-Electron Microscopy Center. A portion of this research was supported by NIH grant U24GM129547 and performed at the PNCC at OHSU and accessed through EMSL (grid.436923.9), a DOE Office of Science User Facility sponsored by the Office of Biological and Environmental Research. A.N. is a Walter Benjamin Fellow funded by the Deutsche Forschungsgemeinschaft (DFG, German Research Foundation) – 464295817. V.C. and T.G. were supported by DFG TRR 152 (P15) and GRK 2338 RTG (P10). A.I.S. is supported by NIH (R01 AR078814, R01 CA206573, R01 NS083660, R01 NS107253).

AUTHOR CONTRIBUTIONS

K.D.N. made constructs, prepared protein samples, and carried out cryo-EM data processing. K.D.N. and A.N. prepared cryo-EM grids. K.D.N. and A.I.S. analyzed structural data. A.I.S. built molecular models. L.C., A.S., T.G., and V.C. performed functional analysis. M.A. and M.G.K. designed computational studies. M.A. performed MD simulations and MD analysis. K.D.N., V.C., and A.I.S. wrote the manuscript, which was then edited by all the authors.

DECLARATION OF INTERESTS

The authors declare no competing interests.

Received: November 20, 2023
Revised: March 7, 2024
Accepted: March 28, 2024

REFERENCES

1. Chubanov, V., Köttgen, M., Touyz, R.M., and Gudermann, T. (2024). TRPM channels in health and disease. Nat. Rev. Nephrol. *20*, 175–187. https://doi.org/10.1038/s41581-023-00777-y.
2. Krapivinsky, G., Krapivinsky, L., Manasian, Y., and Clapham, D.E. (2014). The TRPM7 chanzyme is cleaved to release a chromatin-modifying kinase. Cell *157*, 1061–1072. https://doi.org/10.1016/j.cell.2014.03.046.
3. Nadler, M.J., Hermosura, M.C., Inabe, K., Perraud, A.L., Zhu, Q., Stokes, A.J., Kurosaki, T., Kinet, J.P., Penner, R., Scharenberg, A.M., and Fleig, A. (2001). LTRPC7 is a Mg.ATP-regulated divalent cation channel required for cell viability. Nature *411*, 590–595. https://doi.org/10.1038/35079092.
4. Chubanov, V., Waldegger, S., Mederos y Schnitzler, M., Vitzthum, H., Sassen, M.C., Seyberth, H.W., Konrad, M., and Gudermann, T. (2004). Disruption of TRPM6/TRPM7 complex formation by a mutation in the TRPM6 gene causes hypomagnesemia with secondary hypocalcemia. Proc. Natl. Acad. Sci. USA *101*, 2894–2899. https://doi.org/10.1073/pnas.0305252101.
5. Chubanov, V., Ferioli, S., Wisnowsky, A., Simmons, D.G., Leitzinger, C., Einer, C., Jonas, W., Shymkiv, Y., Bartsch, H., Braun, A., et al. (2016). Epithelial magnesium transport by TRPM6 is essential for prenatal development and adult survival. Elife *5*, e20914. https://doi.org/10.7554/eLife.20914.
6. Mittermeier, L., Demirkhanyan, L., Stadlbauer, B., Breit, A., Recordati, C., Hilgendorff, A., Matsushita, M., Braun, A., Simmons, D.G., Zakharian, E., et al. (2019). TRPM7 is the central gatekeeper of intestinal mineral absorption essential for postnatal survival. Proc. Natl. Acad. Sci. USA *116*, 4706–4715. https://doi.org/10.1073/pnas.1810633116.
7. Schmitz, C., Perraud, A.L., Johnson, C.O., Inabe, K., Smith, M.K., Penner, R., Kurosaki, T., Fleig, A., and Scharenberg, A.M. (2003). Regulation of vertebrate cellular Mg2+ homeostasis by TRPM7. Cell *114*, 191–200. https://doi.org/10.1016/s0092-8674(03)00556-7.
8. Runnels, L.W., Yue, L., and Clapham, D.E. (2001). TRP-PLIK, a bifunctional protein with kinase and ion channel activities. Science *291*, 1043–1047. https://doi.org/10.1126/science.1058519.
9. Monteilh-Zoller, M.K., Hermosura, M.C., Nadler, M.J.S., Scharenberg, A.M., Penner, R., and Fleig, A. (2003). TRPM7 Provides an Ion Channel Mechanism for Cellular Entry of Trace Metal Ions. J. Gen. Physiol. *121*, 49–60. https://doi.org/10.1085/jgp.20028740.
10. Abiria, S.A., Krapivinsky, G., Sah, R., Santa-Cruz, A.G., Chaudhuri, D., Zhang, J., Adstamongkonkul, P., DeCaen, P.G., and Clapham, D.E. (2017). TRPM7 senses oxidative stress to release Zn(2+) from unique intracellular vesicles. Proc. Natl. Acad. Sci. USA *114*, E6079–E6088. https://doi.org/10.1073/pnas.1707380114.
11. Jin, J., Desai, B.N., Navarro, B., Donovan, A., Andrews, N.C., and Clapham, D.E. (2008). Deletion of Trpm7 disrupts embryonic development and thymopoiesis without altering Mg2+ homeostasis. Science *322*, 756–760. https://doi.org/10.1126/science.1163493.
12. Runnels, L.W., Yue, L., and Clapham, D.E. (2002). The TRPM7 channel is inactivated by PIP2 hydrolysis. Nat. Cell Biol. *4*, 329–336. https://doi.org/10.1038/ncb781.
13. Meng, S., Alanazi, R., Ji, D., Bandura, J., Luo, Z.W., Fleig, A., Feng, Z.P., and Sun, H.S. (2021). Role of TRPM7 kinase in cancer. Cell Calcium *96*, 102400. https://doi.org/10.1016/j.ceca.2021.102400.
14. Chubanov, V., and Gudermann, T. (2020). Mapping TRPM7 Function by NS8593. Int. J. Mol. Sci. *21*, 7017. https://doi.org/10.3390/ijms21197017.
15. Ji, D., Fleig, A., Horgen, F.D., Feng, Z.P., and Sun, H.S. (2022). Modulators of TRPM7 and its potential as a drug target for brain tumours. Cell Calcium *101*, 102521. https://doi.org/10.1016/j.ceca.2021.102521.
16. Voringer, S., Schreyer, L., Nadolni, W., Meier, M.A., Woerther, K., Mittermeier, C., Ferioli, S., Singer, S., Holzer, K., Zierler, S., et al. (2020). Inhibition of TRPM7 blocks MRTF/SRF-dependent transcriptional and tumorigenic activity. Oncogene *39*, 2328–2344. https://doi.org/10.1038/s41388-019-1140-8.
17. Liu, H., Dilger, J.P., and Lin, J. (2022). A pan-cancer-bioinformatic-based literature review of TRPM7 in cancers. Pharmacol. Ther. *240*, 108302. https://doi.org/10.1016/j.pharmthera.2022.108302.

18. Rössig, A., Hill, K., Nörenberg, W., Weidenbach, S., Zierler, S., Schaefer, M., Gudermann, T., and Chubanov, V. (2022). Pharmacological agents selectively acting on the channel moieties of TRPM6 and TRPM7. Cell Calcium *106*, 102640. https://doi.org/10.1016/j.ceca.2022.102640.

19. Chubanov, V., Mederos y Schnitzler, M., Meißner, M., Schäfer, S., Abstiens, K., Hofmann, T., and Gudermann, T. (2012). Natural and synthetic modulators of SK (K(ca)2) potassium channels inhibit magnesium-dependent activity of the kinase-coupled cation channel TRPM7. Br. J. Pharmacol. *166*, 1357–1376. https://doi.org/10.1111/j.1476-5381.2012.01855.x.

20. Guan, Z., Chen, X., Fang, S., Ji, Y., Gao, Z., and Zheng, Y. (2021). CCT128930 is a novel and potent antagonist of TRPM7 channel. Biochem. Biophys. Res. Commun. *560*, 132–138. https://doi.org/10.1016/j.bbrc.2021.04.119.

21. Nadezhdin, K.D., Correia, L., Narangoda, C., Patel, D.S., Neuberger, A., Gudermann, T., Kurnikova, M.G., Chubanov, V., and Sobolevsky, A.I. (2023). Structural mechanisms of TRPM7 activation and inhibition. Nat. Commun. *14*, 2639. https://doi.org/10.1038/s41467-023-38362-3.

22. Duan, J., Li, Z., Li, J., Hulse, R.E., Santa-Cruz, A., Valinsky, W.C., Abiria, S.A., Krapivinsky, G., Zhang, J., and Clapham, D.E. (2018). Structure of the mammalian TRPM7, a magnesium channel required during embryonic development. Proc. Natl. Acad. Sci. USA *115*, E8201–E8210. https://doi.org/10.1073/pnas.1810719115.

23. Yelshanskaya, M.V., and Sobolevsky, A.I. (2022). Ligand-Binding Sites in Vanilloid-Subtype TRP Channels. Front. Pharmacol. *13*, 900623. https://doi.org/10.3389/fphar.2022.900623.

24. Koivisto, A.-P., Belvisi, M.G., Gaudet, R., and Szallasi, A. (2022). Advances in TRP channel drug discovery: from target validation to clinical studies. Nat. Rev. Drug Discov. *21*, 41–59. https://doi.org/10.1038/s41573-021-00268-4.

25. Schmidt, E., Narangoda, C., Nörenberg, W., Egawa, M., Rössig, A., Leonhardt, M., Schaefer, M., Zierler, S., Kurnikova, M.G., Gudermann, T., and Chubanov, V. (2022). Structural mechanism of TRPM7 channel regulation by intracellular magnesium. Cell. Mol. Life Sci. *79*, 225. https://doi.org/10.1007/s00018-022-04192-7.

26. Hofmann, T., Schäfer, S., Linseisen, M., Sytik, L., Gudermann, T., and Chubanov, V. (2014). Activation of TRPM7 channels by small molecules under physiological conditions. Pflugers Arch. *466*, 2177–2189. https://doi.org/10.1007/s00424-014-1488-0.

27. Ruan, Z., Haley, E., Orozco, I.J., Sabat, M., Myers, R., Roth, R., Du, J., and Lü, W. (2021). Structures of the TRPM5 channel elucidate mechanisms of activation and inhibition. Nat. Struct. Mol. Biol. *28*, 604–613. https://doi.org/10.1038/s41594-021-00607-4.

28. Liu, C., Reese, R., Vu, S., Rougé, L., Shields, S.D., Kakiuchi-Kiyota, S., Chen, H., Johnson, K., Shi, Y.P., Chernov-Rogan, T., et al. (2021). A Non-covalent Ligand Reveals Biased Agonism of the TRPA1 Ion Channel. Neuron *109*, 273–284.e4. https://doi.org/10.1016/j.neuron.2020.10.014.

29. Nadezhdin, K.D., Neuberger, A., Nikolaev, Y.A., Murphy, L.A., Gracheva, E.O., Bagriantsev, S.N., and Sobolevsky, A.I. (2021). Extracellular cap domain is an essential component of the TRPV1 gating mechanism. Nat. Commun. *12*, 2154. https://doi.org/10.1038/s41467-021-22507-3.

30. Neuberger, A., Oda, M., Nikolaev, Y.A., Nadezhdin, K.D., Gracheva, E.O., Bagriantsev, S.N., and Sobolevsky, A.I. (2023). Human TRPV1 structure and inhibition by the analgesic SB-366791. Nat. Commun. *14*, 2451. https://doi.org/10.1038/s41467-023-38162-9.

31. Nadezhdin, K.D., Neuberger, A., Trofimov, Y.A., Krylov, N.A., Sinica, V., Kupko, N., Vlachova, V., Zakharian, E., Efremov, R.G., and Sobolevsky, A.I. (2021). Structural mechanism of heat-induced opening of a temperature-sensitive TRP channel. Nat. Struct. Mol. Biol. *28*, 564–572. https://doi.org/10.1038/s41594-021-00615-4.

32. Suzuki, S., Penner, R., and Fleig, A. (2020). TRPM7 contributes to progressive nephropathy. Sci. Rep. *10*, 2333. https://doi.org/10.1038/s41598-020-59355-y.

33. Schilling, T., Miralles, F., and Eder, C. (2014). TRPM7 regulates proliferation and polarisation of macrophages. J. Cell Sci. *127*, 4561–4566. https://doi.org/10.1242/jcs.151068.

34. Song, C., Choi, S., Oh, K.B., and Sim, T. (2020). Suppression of TRPM7 enhances TRAIL-induced apoptosis in triple-negative breast cancer cells. J. Cell. Physiol. *235*, 10037–10050. https://doi.org/10.1002/jcp.29820.

35. Luongo, F., Pietropaolo, G., Gautier, M., Dhennin-Duthille, I., Ouadid-Ahidouch, H., Wolf, F.I., and Trapani, V. (2018). TRPM6 is Essential for Magnesium Uptake and Epithelial Cell Function in the Colon. Nutrients *10*, 784. https://doi.org/10.3390/nu10060784.

36. Tian, Y., Yang, T., Yu, S., Liu, C., He, M., and Hu, C. (2018). Prostaglandin E2 increases migration and proliferation of human glioblastoma cells by activating transient receptor potential melastatin 7 channels. J. Cell Mol. Med. *22*, 6327–6337. https://doi.org/10.1111/jcmm.13931.

37. Davis, F.M., Azimi, I., Faville, R.A., Peters, A.A., Jalink, K., Putney, J.W., Jr., Goodhill, G.J., Thompson, E.W., Roberts-Thomson, S.J., and Monteith, G.R. (2014). Induction of epithelial-mesenchymal transition (EMT) in breast cancer cells is calcium signal dependent. Oncogene *33*, 2307–2316. https://doi.org/10.1038/onc.2013.187.

38. Ferioli, S., Zierler, S., Zaißerer, J., Schredelseker, J., Gudermann, T., and Chubanov, V. (2017). TRPM6 and TRPM7 differentially contribute to the relief of heteromeric TRPM6/7 channels from inhibition by cytosolic Mg2+ and Mg·ATP. Sci. Rep. *7*, 8806. https://doi.org/10.1038/s41598-017-08144-1.

39. Baubet, V., Le Mouellic, H., Campbell, A.K., Lucas-Meunier, E., Fossier, P., and Brúlet, P. (2000). Chimeric green fluorescent protein-aequorin as bioluminescent Ca^{2+} reporters at the single-cell level. Proc. Natl. Acad. Sci. USA *97*, 7260–7265. https://doi.org/10.1073/pnas.97.13.7260.

40. Zheng, S.Q., Palovcak, E., Armache, J.P., Verba, K.A., Cheng, Y., and Agard, D.A. (2017). MotionCor2: anisotropic correction of beam-induced motion for improved cryo-electron microscopy. Nat. Methods *14*, 331–332. https://doi.org/10.1038/nmeth.4193.

41. Kimanius, D., Forsberg, B.O., Scheres, S.H., and Lindahl, E. (2016). Accelerated cryo-EM structure determination with parallelisation using GPUs in RELION-2. Elife *5*, e18722. https://doi.org/10.7554/eLife.18722.

42. Punjani, A., Rubinstein, J.L., Fleet, D.J., and Brubaker, M.A. (2017). cryoSPARC: algorithms for rapid unsupervised cryo-EM structure determination. Nat. Methods *14*, 290–296. https://doi.org/10.1038/nmeth.4169.

43. Pettersen, E.F., Goddard, T.D., Huang, C.C., Couch, G.S., Greenblatt, D.M., Meng, E.C., and Ferrin, T.E. (2004). UCSF Chimera—A visualization system for exploratory research and analysis. J. Comput. Chem. *25*, 1605–1612. https://doi.org/10.1002/jcc.20084.

44. Pettersen, E.F., Goddard, T.D., Huang, C.C., Meng, E.C., Couch, G.S., Croll, T.I., Morris, J.H., and Ferrin, T.E. (2021). UCSF ChimeraX: Structure visualization for researchers, educators, and developers. Protein Sci. *30*, 70–82. https://doi.org/10.1002/pro.3943.

45. (2002). The PyMOL Molecular Graphics System (DeLano Scientific).

46. Afonine, P.V., Grosse-Kunstleve, R.W., Echols, N., Headd, J.J., Moriarty, N.W., Mustyakimov, M., Terwilliger, T.C., Urzhumtsev, A., Zwart, P.H., and Adams, P.D. (2012). Towards automated crystallographic structure refinement with phenix.refine. Acta Crystallogr. D *68*, 352–367. https://doi.org/10.1107/s0907444912001308.

47. Emsley, P., Lohkamp, B., Scott, W.G., and Cowtan, K. (2010). Features and development of Coot. Acta Crystallogr. D *66*, 486–501. https://doi.org/10.1107/s0907444910007493.

48. Jo, S., Kim, T., Iyer, V.G., and Im, W. (2008). CHARMM-GUI: A web-based graphical user interface for CHARMM. J. Comput. Chem. *29*, 1859–1865. https://doi.org/10.1002/jcc.20945.

49. Wu, E.L., Cheng, X., Jo, S., Rui, H., Song, K.C., Dávila-Contreras, E.M., Qi, Y., Lee, J., Monje-Galvan, V., Venable, R.M., et al. (2014). CHARMM-GUI *Membrane Builder* toward realistic biological membrane simulations. J. Comput. Chem. *35*, 1997–2004. https://doi.org/10.1002/jcc.23702.

50. Case, D.A., Cheatham, T.E., Darden, T., Gohlke, H., Luo, R., Merz, K.M., Onufriev, A., Simmerling, C., Wang, B., and Woods, R. (2005). The Amber biomolecular simulation programs. J. Computat. Chem. *26*, 1668–1688.

51. Roe, D.R., and Cheatham, T.E. (2013). PTRAJ and CPPTRAJ: Software for Processing and Analysis of Molecular Dynamics Trajectory Data. J. Chem. Theory Comput. *9*, 3084–3095. https://doi.org/10.1021/ct400341p.

52. Humphrey, W., Dalke, A., and Schulten, K. (1996). VMD: Visual molecular dynamics. J. Mol. Graph. *14*, 33–38. https://doi.org/10.1016/0263-7855(96)00018-5.

53. Scheres, S.H.W. (2012). RELION: Implementation of a Bayesian approach to cryo-EM structure determination. J. Struct. Biol. *180*, 519–530. https://doi.org/10.1016/j.jsb.2012.09.006.

54. Smart, O.S., Neduvelil, J.G., Wang, X., Wallace, B.A., and Sansom, M.S. (1996). HOLE: a program for the analysis of the pore dimensions of ion channel structural models. J. Mol. Graph. *14*, 354–360, 376. https://doi.org/10.1016/s0263-7855(97)00009-x.

55. Held, K., Kichko, T., De Clercq, K., Klaassen, H., Van Bree, R., Vanherck, J.C., Marchand, A., Reeh, P.W., Chaltin, P., Voets, T., and Vriens, J. (2015). Activation of TRPM3 by a potent synthetic ligand reveals a role in peptide release. Proc. Natl. Acad. Sci. USA *112*, E1363–E1372. https://doi.org/10.1073/pnas.1419845112.

56. McKemy, D.D., Neuhausser, W.M., and Julius, D. (2002). Identification of a cold receptor reveals a general role for TRP channels in thermosensation. Nature *416*, 52–58. https://doi.org/10.1038/nature719.

57. Wang, J., Wolf, R.M., Caldwell, J.W., Kollman, P.A., and Case, D.A. (2004). Development and testing of a general amber force field. J. Comput. Chem. *25*, 1157–1174. https://doi.org/10.1002/jcc.20035.

58. Dickson, C.J., Madej, B.D., Skjevik, A.A., Betz, R.M., Teigen, K., Gould, I.R., and Walker, R.C. (2014). Lipid14: The Amber Lipid Force Field. J. Chem. Theory Comput. *10*, 865–879. https://doi.org/10.1021/ct4010307.

59. Ryckaert, J.-P., Ciccotti, G., and Berendsen, H.J. (1977). Numerical integration of the cartesian equations of motion of a system with constraints: molecular dynamics of n-alkanes. J. Comput. Phys. *23*, 327–341. https://doi.org/10.1016/0021-9991(77)90098-5.

60. Laskowski, R.A., and Swindells, M.B. (2011). LigPlot+: Multiple Ligand–Protein Interaction Diagrams for Drug Discovery. J. Chem. Inf. Model. *51*, 2778–2786. https://doi.org/10.1021/ci200227u.

STAR★METHODS

KEY RESOURCES TABLE

REAGENT or RESOURCE	SOURCE	IDENTIFIER
Chemicals, peptides, and recombinant proteins		
Penicillin-Streptomycin	Merck	Cat# P4333
Icilin	Tocris	Cat# 1531
Coelenterazine	Carl Roth	Cat# 4094.3
Kanamycin	Fisher scientific	Cat# BP906-5
Tetracycline	Fisher scientific	Cat# BP912
Naltriben	Merck	Cat# N156
VER155008	Tocris	Cat# 3803
IPTG	Zymo Research	Cat# I1001-5
Tris	Fisher scientific	Cat# BP152-1
NaCl	Fisher scientific	Cat# BP358-212
CCT128930 (in cryo-EM)	Cayman Chemical Company	Cat# 18194
CCT128930 (in functional experiments)	Selleckchem	#CCT128930
CIM 0216	Tocris	Cat# 5521
NS8593	Tocris	Cat# 4597
PMSF	Acros Organics	Cat# 215740500
2-Mercaptoethanol (βME)	Acros Organics	Cat# 125470100
Phosphate-Buffered Saline	Corning	Cat# 21-040-CV
Bio-beads SM-2	Bio-Rad	Cat# 152-8920
D-desthiobiotin	Sigma	Cat# D1411
Glyco-diosgenin (GDN)	Anatrace	Cat# GDN101
POPC:POPE:POPG	Anatrace	Cat# P516:P416:P616
Ruthenium red	Tocris	Cat# 11103-72-3
Sf-900 III SFM	Thermo Fisher Scientific	Cat# 12658027
Freestyle 293 expression medium	Thermo Fisher Scientific	Cat# 12338018
Sodium butyrate	ACROS Organics	Cat# 263191000
QuikChange II XL Site-Directed Mutagenesis Kit	Agilent	Cat# 200521
DMEM	Merck	Cat# D6429
Deposited data		
Coordinates of $TRPM7_{CCT}$	This paper	PDB ID: 8W2L
Cryo-EM density map of $TRPM7_{CCT}$	This paper	EMDB: EMD-43751
Experimental models: cell lines		
HEK293S GnTI^{-}	ATCC	Cat# CRL-3022
Sf9	Gibco	Cat# 12659017
HEK293T	ATCC	Cat# CRL3216
Recombinant DNA		
Mouse *Trpm7* cDNA (a.a. 1–1280)	Nadezhdin et al.[21]	N/A
Mouse *Trpm7* cDNA in *pIRES2-EGFP* vector (plasmid)	Ferioli et al.[38]	NM_021450
Mouse *Trpm6* cDNA in *pIRES2-EGFP* vector (plasmid)	Ferioli et al.[38]	KX375810
Mouse *Trpm3* cDNA in *pcDNA3.1-TOPO* vector (plasmid)	Chubanov et al.[19]	JF706722
Human *TRPM8* cDNA in *pcDNA3.1-TOPO* vector (plasmid)	Chubanov et al.[19]	NM_076985

(*Continued on next page*)

Continued		
REAGENT or RESOURCE	SOURCE	IDENTIFIER
EGFP fused to Aequorea victoria aequorin in *pG5A* vector (plasmid)	Baubet et al.[39]	N/A
Oligonucleotides		
Forward primer for *Trpm7-D922E:* 5′-tgtgtcactgacattgaagtactcgctaaaccatactttaatc-3′	This paper	N/A
Reverse primer for *Trpm7-D922E:* 5′-gattaaagtatggtttagcgagtacttcaatgtcagtgacaca-3′	This paper	N/A
Forward primer for *Trpm7-F924W:* 5′-ggcaattgtgtcactgacattccagtagtcgctaaaccatactt-3′	This paper	N/A
Reverse primer for *Trpm7-F924W:* 5′-aagtatggtttagcgactactggaatgtcagtgacacaattgcc-3′	This paper	N/A
Forward primer for *Trpm7-F924A:* 5′-ggcaattgtgtcactgacattggcgtagtcgctaaaccatacttta-3′	This paper	N/A
Reverse primer for *Trpm7-F924A:* 5′-taaagtatggtttagcgactacgccaatgtcagtgacacaattgcc-3	This paper	N/A
Software and algorithms		
SerialEM 4.0		https://bio3d.colorado.edu/SerialEM
Motioncor2	Zheng et al.[40]	http://msg.ucsf.edu/em/software/motioncor2.html
Relion 4.0	Kimanius et al.[41]	http://www2.mrc-lmb.cam.ac.uk/relion/
cryoSPARC 4.3.0	Punjani et al.[42]	https://cryosparc.com/
UCSF Chimera	Pettersen et al.[43]	https://www.cgl.ucsf.edu/chimera/
UCSF ChimeraX	Pettersen et al.[44]	https://www.cgl.ucsf.edu/chimerax/
Pymol (Schrödinger)	DeLano Scientific[45]	http://www.pymol.org
PHENIX	Afonine et al.[46]	https://www.phenix-online.org/
COOT	Emsley et al.[47]	http://www2.mrc-lmb.cam.ac.uk/Personal/pemsley/coot
CHARMM-GUI	Jo et al., Wu et al.[48,49]	https://charmm-gui.org/
AmberTools20	Case et al.[50]	https://ambermd.org/AmberTools.php
CPPTRAJ	Roe and Cheatham[51]	https://amberhub.chpc.utah.edu/cpptraj/
VMD 1.9.4	Humphrey et al.[52]	https://www.ks.uiuc.edu/Research/vmd/
PatchMaster V2x69	Harvard Bioscience	www.heka.com
GraphPad Prism 10.11	GraphPad Software	www.graphpad.com
Other		
UltrAuFoil R1.2/1.3 -Au 300 mesh, Gold	Ted Pella (Quantifoil)	Cat# 688-300-AU-50
Size Exclusion Superose 10/300 column	GE Healthcare	Cat# 17-5172-01

RESOURCE AVAILABILITY

Lead contact

Further information and requests for the resources and reagents should be directed to and will be fulfilled by the lead contact, Alexander Sobolevsky (as4005@cumc.columbia.edu).

Materials availability

Materials listed in key resources table under ‘‘Recombinant DNA’’ and ‘‘Oligonucleotides’’ should be requested from the lead contact, Alexander Sobolevsky (as4005@cumc.columbia.edu). Unique reagents generated in the study will be available upon MTA completion.

Data and code availability

- The cryo-EM map for $TRPM7_{CCT}$ has been deposited in the Electron Microscopy Data Bank under the accession code EMD-43751. The coordinates for the atomic model of $TRPM7_{CCT}$ have been deposited in the Protein Data Bank under the accession code 8W2L.
- This paper does not report original code.
- Any additional information required to reanalyze the data reported in this paper is available from the lead contact upon request.

EXPERIMENTAL MODEL AND STUDY PARTICIPANT DETAILS

Cell lines

For structural experiments, expression of mouse TRPM7 was performed in HEK293S cells lacking N-acetyl-glucosaminyltransferase I ($GnTI^-$, mycoplasma test negative, ATCC #CRL-3022) that were maintained at 37°C and 6% CO_2 in Freestyle 293 medium (Thermo Fisher Scientific #12338-018) supplemented with 2% FBS. Baculovirus for infecting HEK293S $GnTI^-$ cells was produced in Sf9 cells (GIBCO) cultured in the Sf-900 III SFM media (GIBCO) at 27°C. For aequorin-based Ca^{2+} influx assay and patch-clamp experiments, TRPM channels were expressed in HEK293T cells (mycoplasma test negative, ATCC #CRL3216) that were maintained at 37°C and 5% CO_2 in DMEM (Merck, #D6429) supplemented with 10% fetal calf serum (Thermo Fisher Scientific, #10270106), 100 μg/ml streptomycin and 100 U/ml penicillin (Merck, #P4333).

METHOD DETAILS

Constructs

For structural experiments, cDNA for mouse *Trpm7* (NM_021450) truncated C-terminally (the corresponding protein residues 1–1280)[22,25] was introduced into the *pEG-BacMam* vector for protein expression in mammalian cells, with an N-terminal region coding for the streptavidin affinity tag (residues WSHPQFEK), followed by the green fluorescent protein (GFP) and thrombin cleavage site (residues LVPRG), as described before.[21] For functional experiments, full-length mouse *Trpm7* (NM_021450) and *Trpm6* (KX375810) were introduced into the *pIRES2-EGFP* expression vector as reported previously.[18,25] Point mutations D922E, F924W and F924A in *Trpm7* were introduced using the QuikChange II XL Site-Directed Mutagenesis Kit (Agilent) according to the manufacturer's protocol and verified by sequencing (Eurofins, Germany). The *Trpm7* variants with A981L, A981V and W1111A mutations were described earlier.[21] Mouse *Trpm3* cDNA (JF706722; in *pcDNA3.1-TOPO* vector) and human *TRPM8* (NM_076985; in *pcDNA3.1-TOPO* vector) were described earlier.[19]

Protein expression and purification

For cryo-EM studies, TRPM7 bacmids and baculoviruses were produced using the standard procedures.[21] Briefly, baculoviruses were made in Sf9 cells (Thermo Fisher Scientific, mycoplasma test negative, #12659017) for ~96 hours and added to suspension-adapted HEK293S $GnTI^-$ cells. To reduce TRPM7 cytotoxicity, 10 μM ruthenium red was added to the suspension of HEK293S $GnTI^-$ cells. To enhance protein expression, sodium butyrate (10 mM) was added 12 hours after transduction, and the temperature was reduced to 30°C. The cells were harvested 48 hours after transduction by 15-min centrifugation at 5,471 g using a Sorvall Evolution RC centrifuge (Thermo Fisher Scientific). The cells were washed in the phosphate-buffered saline (PBS) pH 7.4 and pelleted by centrifugation at 3,202 g for 10 min using an Eppendorf 5810 centrifuge.

The cell pellet was resuspended in the ice-cold buffer containing 20 mM Tris pH 8.0, 150 mM NaCl, 0.8 μM aprotinin, 4.3 μM leupeptin, 2 μM pepstatin A, 1 μM phenylmethylsulfonyl fluoride (PMSF), and 1 mM β-mercaptoethanol (βME). The suspension was supplemented with 1% (w/v) glyco-diosgenin (GDN), and the cells were lysed at constant stirring for 2 hours at 4°C. Unbroken cells and cell debris were pelleted in the Eppendorf 5810 centrifuge at 3,202 g and 4°C for 10 min. Insoluble material was removed by ultracentrifugation for 1 hour at 186,000 g in a Beckman Coulter centrifuge using a 45 Ti rotor. The supernatant was added to the strep resin, which was then rotated for 20 min at 4°C. The resin was washed with 10 column volumes of the wash buffer containing 20 mM Tris pH 8.0, 150 mM NaCl, 1 mM βME, and 0.01% (w/v) GDN, and the protein was eluted with the same buffer supplemented with 2.5 mM D-desthiobiotin. The eluted protein was concentrated to 0.5 ml using a 100-kDa NMWL centrifugal filter (MilliporeSigma™ Amicon™) and then centrifuged in a Sorvall MTX 150 Micro-Ultracentrifuge (Thermo Fisher Scientific) for 30 min at 66,000 g and 4°C using a S100AT4 rotor before injecting it into a size-exclusion chromatography (SEC) column. The protein was purified using a Superose™ 6 10/300 GL SEC column attached to an AKTA FPLC (GE Healthcare) and equilibrated with the buffer containing 150 mM NaCl, 20 mM Tris pH 8.0, 1 mM βME, and 0.01% (w/v) GDN. The tetrameric peak fractions were pooled and concentrated to 2–3 mg/ml using the 100-kDa NMWL centrifugal filter.

For TRPM7 reconstitution into MSP2N2 nanodiscs, the purified TRPM7 protein was mixed with the purified MSP2N2 protein and lipids POPC:POPE:POPG (3:1:1, molar ratio; 1-palmitoyl-2-oleoyl-glycero-3-phosphocholine – POPC, 1-palmitoyl-2-oleoyl-glycero-3-phosphoethanolamine – POPE, 1-palmitoyl-2-oleoyl-glycero-3-phosphoglycerol – POPG; Anatrace) at a molar ratio of 1:3:166 (monomer:MSP2N2:lipid). The MSP2N2 protein was stored in a buffer containing 150 mM NaCl and 20 mM Tris (pH 8.0). The lipids were resuspended to a concentration of 100 mg/mL in 150 mM NaCl, 20 mM Tris (pH 8.0) and subjected to 5–10 cycles of freezing in liquid nitrogen and thawing in a water bath sonicator. The nanodisc mixture (500 μL) was rocked at room temperature for 1 hour.

Subsequently, the nanodisc mixture was supplemented with 40 mg of Bio-beads SM2 (Bio-Rad) pre-wet in the buffer containing 20 mM Tris pH 8.0, 150 mM NaCl, and 1 mM βME and subjected to rotation at 4°C. After one hour of rotation, 40 mg more of Bio-beads SM2 was added, and the resulting mixture was rotated at 4°C for another ~14–20 hours. The Bio-beads SM2 were then removed by pipetting, and TRPM7 reconstituted in nanodiscs was purified from empty nanodiscs by SEC using the Superose™ 6 10/300 GL column equilibrated in the buffer containing 150 mM NaCl, 20 mM Tris (pH 8.0), and 1 mM βME. The SEC fractions corresponding to TRPM7 reconstituted into nanodiscs were pooled and concentrated to 1.9 mg/ml using the 100-kDa NMWL centrifugal filter.

Cryo-EM sample preparation and data collection

The nanodisc-reconstituted TRPM7 was supplemented with 400 μM of CCT128930, which was then incubated for 15 minutes at room temperature before grid freezing. CCT was acquired from Cayman Chemical Company. Before sample application, UltrAuFoil R 1.2/1.3, Au 300 (300-mesh) grids were plasma treated in a PELCO easiGlow glow discharge cleaning system (0.39 mBar, 15 mA, "glow" for 25 s, and "hold" for 10 s). A Mark IV Vitrobot (Thermo Fisher Scientific) set to 100% humidity and 4°C was used to plunge-freeze the grids in liquid ethane after applying 3 μl of protein sample to their gold-coated side using the blot time of 3 s, blot force of 3, and wait time of 15 s. The grids were stored in liquid nitrogen before imaging.

Images of frozen-hydrated particles of TRPM7 in the presence of 400 μM CCT were collected on a Titan Krios transmission electron microscope (Thermo Fisher Scientific) operating at 300 kV and equipped with a Gatan K3 Summit direct electron detection camera (Gatan, Pleasanton, CA, USA) using SerialEM 4.0. A total of 9,254 micrographs were collected in the super-resolution mode with a physical-resolution pixel size of 0.788 Å (super-resolution pixel size 0.394 Å) across the defocus range of −0.75 to −1.5 μm. The total dose of ~60 $e^{-}Å^{-2}$ was attained by using the dose rate of ~15 $e^{-}pixel^{-1}s^{-1}$ across 50 frames during the 2.48-s exposure time.

Image processing and 3D reconstruction

Single-particle cryo-EM data was processed in cryoSPARC 4.3.0[42] and Relion 4.0.[53] Movie frames were aligned using the MotionCor2 algorithm implemented in Relion 4.0. The contrast transfer function (CTF) estimation was performed using the patch CTF estimation in cryoSPARC 4.3.0. Following CTF estimation, micrographs were manually inspected and those with outliers in defocus values, ice thickness, and astigmatism as well as micrographs with lower predicted CTF-correlated resolution were excluded from further processing (individually assessed for each parameter relative to the overall distribution). The total number of 4,800,731 particles were picked using internally generated 2D templates and, after inspection, 3,969,671 particles were extracted with the 360-pixel box size and then binned to the 128-pixel box size. After several rounds of reference-free 2D classifications and Heterogeneous Refinements in cryoSPARC with one reference class and three automatically generated "garbage" classes, the best 759,539 particles were imported into Relion and re-extracted with the 360-pixel box size and binned to the 256-pixel box size. These particles were subjected to one round of 3D classification into 10 classes without imposing symmetry restraints (C1 symmetry). Particles representing the best classes were combined, refined together (C1) and subjected to CTF refinements to correct for the beam-tilt, higher order aberrations, anisotropic magnification, per particle defocus, and per micrograph astigmatism.[42] The CTF-refined particles were subjected to Bayesian polishing and CTF refined again using the same procedure as described above. Polished and CTF-refined particles (433,014) were imported into cryoSPARC. The final set of 433,014 particles representing the best classes was subjected to homogenous, non-uniform, and CTF refinements with C4 rotational symmetry. The reported resolution of 2.45 Å for the final map was estimated using the gold standard Fourier shell correlation (GSFSC) using FSC = 0.143 criterion. Cryo-EM density was visualized using UCSF Chimera[43] and ChimeraX.[44]

Model building

The $TRPM7_{CCT}$ model was built in Coot[47] using the previously published cryo-EM structure of TRPM7 (PDB ID: 8SI3) as a guide. The model was tested for overfitting by shifting the coordinates by 0.5 Å (using Shake) in Phenix,[46] refining the shaken model against the corresponding unfiltered half map, and generating densities from the resulting model in UCSF Chimera. The resulting model was real space refined in Phenix 1.18 and visualized using UCSF Chimera and PyMOL (The PyMOL Molecular Graphics System, Version 2.0 Schrödinger, LLC.). The pore radius was calculated using HOLE.[54]

Aequorin-based Ca^{2+} influx assay

Measurements of $[Ca^{2+}]_i$ in TRPM7 expressing cells were performed as reported previously,[18,21,25] with several modifications. HEK293T cells cultured in 6-well plates (~60% confluence) were transfected with 2 μg/dish *Trpm7* plasmid DNA and 0.1 μg/dish *pG5A* plasmid DNA encoding EGFP fused to *Aequorea victoria* aequorin, using Lipofectamine 2000 (Thermo Fisher Scientific, #11668019). Twenty-four hours after transfection, the cells were washed with Mg^{2+}-free HEPES-buffered saline (Mg^{2+}-free HBS) containing 150 mM NaCl, 5.4 mM KCl, 0.5 mM $CaCl_2$, 5 mM HEPES (pH 7.4) and 10 mM glucose, and mechanically resuspended in the Mg^{2+}-free HBS. For reconstitution of aequorin, cell suspensions were incubated with 5 μg/ml coelenterazine (Carl Roth, #4094.3) in the Mg^{2+}-free HBS for 30 min at room temperature. Cells were washed twice by centrifugation at 2000 rpm for 5 min (Heraeus Pico 17 microcentrifuge, Thermo Fisher Scientific), resuspended in the Mg^{2+}-free HBS and aliquoted into 96-well plates ($1x10^5$ cells per well). Luminescence was detected at room temperature using a CLARIOstar microplate reader (BMG LABTECH GmbH). To monitor the effects of CCT, NS8593 (NS; Tocris, #4597) and VER155008 (VER; Tocris, #3803), the extracellular concentration of Ca^{2+}

was increased to 5 mM by injecting the $CaCl_2$-containing Mg^{2+}-free HBS in the absence or presence of the inhibitors. The background Ca^{2+} influx was determined using cells transfected with an inactive mutant channel *Trpm7-P1040R*.[21,25] To study activation by naltriben (NTB; Tocris, #N156), TRPM7-transfected cells were exposed to Mg^{2+}-free HBS containing different concentrations of the agonist. The experiments were terminated by lysing cells with 0.05% (v/v) Triton X-100 in the Mg^{2+}-free HBS to record the total bioluminescence. The bioluminescence rates (counts/s) were analyzed at 1-s intervals and calibrated as $[Ca^{2+}]_i$ values using the following equation:

$$p[Ca^{2+}]_i = 0.332588\,(-log(k)) + 5.5593 \quad \text{(Equation 1)}$$

where *k* represents the rate of aequorin consumption, i.e., counts/s divided by the total number of counts.

The concentration dependencies for inhibitors CCT, NS and VER were fitted with the following logistic equation:

$$E(c) = E_{min} + \frac{E_{max} - E_{min}}{1 + \frac{c^h}{IC_{50}{}^h}} \quad \text{(Equation 2)}$$

where *E(c)* is TRPM7 activity at the concentration *c* of the compound, E_{min} is the minimal activity, E_{max} is the maximal activity, IC_{50} is the half-maximal inhibitory concentration, and *h* is the Hill coefficient. Similarly, the concentration dependencies for agonist NTB were fitted with the following logistic equation:

$$E(c) = E_{min} + \frac{E_{max} - E_{min}}{1 + \frac{EC_{50}{}^h}{c^h}} \quad \text{(Equation 3)}$$

where EC_{50} is the half-maximal effective concentration.

Assessment of HEK293T cells expressing TRPM3 and TRPM8 were performed analogously to the experiments with TRPM6 and TRPM7 except that HEPES-buffered saline contained 2 mM Ca^{2+} and 1 mM Mg^{2+}. TRPM3 was stimulated by an external application of CIM 0216 (Tocris, #5521).[55] TRPM8 was activated by icilin (Tocris, #1531).[56]

Patch-clamp measurements

Patch-clamp experiments with TRPM6 and TRPM7 were performed as reported previously,[18,21,25] with a few modifications. HEK293T cells grown in 35-mm dishes to ~60% confluence were transiently transfected with *Trpm7* cDNAs or *Trpm6* in the *pIRES2-EGFP* vector (2 μg/dish). Patch-clamp experiments were conducted 18-22 hours after transfection with cells displaying EGFP fluorescence. Whole-cell currents were recorded using an EPC10 patch-clamp amplifier and PatchMaster software (Version V2x69, Harvard Bioscience). Voltages were corrected for a liquid junction potential of 10 mV. Currents were elicited by voltage ramps from –100 mV to +100 mV over 50 ms applied every 2 seconds. The inward and outward current amplitudes were measured at –80 mV and +80 mV and were normalized to the cell size as pA/pF. The capacitance was measured using the automated capacitance cancellation function of EPC10. The standard extracellular solution contained 140 mM NaCl, 2.8 mM KCl, 1 mM $CaCl_2$, 2 mM $MgCl_2$, 10 mM HEPES-NaOH, and 11 mM glucose (all from Merck). Solutions were adjusted to pH 7.2 using an FE20 pH meter (Mettler Toledo) and to 290 mOsm using a Vapro 5520 osmometer (Wescor Inc). Patch pipettes were made of borosilicate glass (Science Products) and had a resistance of 2.0−3.7 MΩ when filled with the standard intracellular pipette solution containing 120 mM Cs-glutamate, 8 mM NaCl, 10 mM Cs-EGTA, 5 mM Cs-EDTA, and 10 mM HEPES-CsOH. The intracellular solution was also adjusted to pH 7.2 and 290 mOsm.

System preparation for molecular dynamics simulations

Initial atomic coordinates for Molecular Dynamics (MD) simulations were obtained from the $TRPM7_{CCT}$, $TRPM7_{VER}$, $TRPM7_{NS}$ and $TRPM7_{apo}$ structures. Each structure was truncated to include the TMD and TRP helices (residues 843−1147 of the protein, 843−1141 for $TRPM7_{CCT}$ due to the missing residues). Each simulation box was constructed in CHARMM-GUI membrane builder[48,49] by inserting the truncated protein into a POPC bilayer and solvating with TIP3P water molecules and 150 mM NaCl. The systems were set up for MD simulations using the "tleap" module of the AmberTools20 package.[50] Parametrization of all the ligands was carried out using the general AMBER force field (GAFF).[57] Total number of atoms in the final simulation boxes was 181,313 for $TRPM7_{CCT}$ system, 184,906 for $TRPM7_{VER}$ system, 184,188 for $TRPM7_{NS}$ system and 183,380 for $TRPM7_{apo}$ system. The boxes contained 34,124, 35,311, 35,189 and 34,973 water molecules for $TRPM7_{CCT}$, $TRPM7_{VER}$, $TRPM7_{NS}$ and $TRPM7_{apo}$ systems, respectively. $TRPM7_{CCT}$ system contained 96 Na^+ and 114 Cl^- ions while other systems contained 95 Na^+ and 117 Cl^- ions. The number of lipid molecules was 435 for $TRPM7_{CCT}$ system, 432 for $TRPM7_{VER}$ system and 430 for $TRPM7_{NS}$ and $TRPM7_{apo}$ systems.

Molecular dynamics simulation protocols

"pmemd.cuda" program of the Amber20 molecular dynamics software package was used for all MD simulations.[50] Amber FF99SB–ILDN force field parameters were used for protein and ions, TIP3P model for water, and Lipid14[58,59] force field parameters for lipids.

All equilibration and production simulations were performed in NPT ensemble at 300 K temperature and 1 bar pressure with anisotropic pressure scaling. The temperature was controlled using Langevin thermostat with a collision frequency of 1 ps^{-1} and the pressure was controlled using Berendsen barostat with a relaxation time of 1 ps as implemented in Amber20. All covalent bonds involving hydrogen atoms were constrained using the SHAKE algorithm,[59] with the integration time step of 2 fs. The electrostatic interactions were approximated using the Particle Mesh Ewald (PME) method, with a non-bonded interaction cutoff radius of 10 Å. Periodic boundary conditions were applied in all directions.

Each system was minimized and heated from 0.1 K to 100 K at the constant volume and from 100 to 300 K at the constant pressure, with all protein main-chain heavy atoms and ligand heavy atoms (for $TRPM7_{CCT}$, $TRPM7_{VER}$ and $TRPM7_{NS}$ systems) harmonically restrained at their original positions with the force constant of 20 kcal mol^{-1} $Å^{-2}$. The systems were then equilibrated for 160 ns, gradually releasing the restraints on the protein and the ligand. To limit excessive fluctuations of the protein due to the truncation, the Cα atoms in the terminal regions (residues 843–850 and 1134–1147) were restrained with the force constant of 5 kcal mol^{-1} $Å^{-2}$ throughout production simulations. For all the models, the backbone N-O distances of the TRP helix residues 1109–1123 were additionally restrained between 2.60−2.80 and 4.0−4.50 Å. All the other restraints were removed for the production runs. Production simulations were carried out for 800–950 ns.

Molecular dynamics trajectory analysis

Post-processing and analysis of the trajectories were carried out using CPPTRAJ[51] module of AmberTools20 and VMD 1.9.4.[52] VMD 1.9.4 was used to visualize trajectories and generate molecular graphics.

QUANTIFICATION AND STATISTICAL ANALYSIS

Fitting of dose-response curves was performed using GraphPad Prism 10.11. The results were tested for normal distribution using the Shapiro-Wilk test followed by unpaired t test with Welch's correction, paired t test or U test (Mann-Whitney) using GraphPad Prism 10.11 as indicated in the figure legends. The significance was accepted at $p \leq 0.05$ and data are presented as the means ± SEM. The statistical details of experiments can be found in figure legends (Figures 1, 2, 3, 4, 6, S1, and S6) and in the results. Quantification of TRPM7-inhibitor interaction distances was performed using LigPlot.[60]